Available online at www.sciencedirect.com
SCIENCE DIRECT®
Pergamon
Cement and Concrete Research 34 (2004) 1459–1466
CEMENT AND CONCRETE RESEARCH

Magnetic resonance imaging of crack formation in hydrated cement paste materials

J.J. Young[a,b], P. Szomolanyi[a], T.W. Bremner[b,*], B.J. Balcom[a,*]

[a]Department of Physics, MRI Centre, P.O. Box 4400, University of New Brunswick, Fredericton, New Brunswick, Canada E3B 5A3
[b]Department of Civil Engineering, P.O. Box 4400, University of New Brunswick, Fredericton, New Brunswick, Canada E3B 5A3

Received 27 January 2003; accepted 29 January 2004

Abstract

A magnetic resonance imaging (MRI) methodology is presented to spatially resolve cracking in hydrated cement paste. The method is based on the relatively long spin–lattice (T_1) and spin–spin relaxation (T_2) times (magnetic resonance signal lifetimes) associated with water-filled cracks. Water-filled capillary and gel pores have much shorter signal lifetimes. As a noninvasive method, the technique may be used to study crack formation and propagation in well-controlled laboratory test samples. The method is proven to be capable of spatially resolving crack structures with widths of tens of micrometers.

Keywords: Hydration; Crack detection; Pore size distribution; Cement paste; Magnetic resonance imaging

1. Introduction

Extensive cracking of cement-based materials, such as concrete, is a major durability problem [1]. Limiting cracking of concrete is desirable, thereby preventing easy access of aggressive ions into the interior of the concrete and as a result, producing a more durable building material. ACI Committee 224R-90 has recognized that some cracking will occur and they have set crack width limits based on the exposure conditions of the structure. In addition to structural cracking, there are many other sources of cracking, such as drying shrinkage, plastic shrinkage, freeze/thaw damage, and expansive alkali–aggregate reactions. All of these types of cracking are potential durability concerns, irrespective of the mechanism causing the cracking.

Hornain et al. [2] have defined the properties which would be desired of any method proposed to study cracking in cement-based materials. They suggested that an ideal method should not induce further cracking, it should be simple, economic, and in addition, should be rapid and provide high resolution. Finally, they suggested an ideal technique should be able to characterize the initial state of the material [3] and should be coupled with an image analysis system. In this paper, we introduce a new magnetic resonance imaging (MRI) methodology to distinguish cracks from water held in the pore structure of cement paste. The relatively long spin–lattice relaxation (T_1) and spin–spin relaxation (T_2) times characteristic of cracks form the basis of our new crack detection methodology.

2. Theory

MRI is a flexible technique because of the large number of variables to which it is sensitive, for example, proton density, molecular environment, molecular dynamics, signal lifetimes, chemical composition, and temperature [4]. There are three principal relaxation times associated with the MR phenomena: T_1, T_2, and effective spin–spin relaxation (T_2*). Each of these relaxation times are sample dependant and to some degree hardware or system dependant. Previous research has shown that the bulk T_1 and T_2 of the liquid water phase in hydrated white portland cement pastes are generally multiexponential and on the order of a few milliseconds and hundreds of microseconds, respectively [5]. The T_2* relaxation time is related to T_2 and substantially

* Co-corresponding authors. T.W. Bremner is to be contacted at the Department of Civil Engineering, University of New Brunswick, P.O. Box 4400, Fredericton, New Brunswick, Canada E3B 5A3. B.J. Balcom is to be contacted at the Department of Physics, MRI Centre, University of New Brunswick, 8 Bailey Drive, P.O. Box 4400, Fredericton, New Brunswick, Canada E3B 5A3. Tel.: +1-506-458-7938; fax: +1-506-453-4581.
E-mail address: bjb@unb.ca (B.J. Balcom).

0008-8846/$ – see front matter © 2004 Elsevier Ltd. All rights reserved.
doi:10.1016/j.cemconres.2004.01.023

influenced by sample-induced inhomogeneities in the magnetic field, with typical values on the order of hundreds of microseconds in white portland-cement-based materials [6].

The T_1 and T_2 relaxation parameters in porous materials are generally accepted to be related to the surface to volume ratio (S/V) of water-bearing pores as described by Eqs. (1) and (2) [7]. The parameters ρ_1 and ρ_2 are the spin–lattice and spin–spin surface relaxivity constants. S and V are the surface area and volume of a pore respectively, which define the S/V ratio. The fact that T_1 and T_2 are related to the S/V ratio has been used by Plassais et al. [8], Jehng et al. [9], and Halperin et al. [10] to determine pore size distributions in hydrated cement pastes. Beyea et al. [6,11] have found changes in relaxation times as a result of drying and they attribute this change to microcracking. Cement paste contains a distribution of pore sizes that range from the nanometer size up the micrometer scale [12]. Assuming the S/V ratio in these pores can be estimated as the S/V ratio of a sphere; as the pore size decreases, the T_1 and T_2 signal lifetimes decrease. A distribution in pore size, related through the S/V ratio, naturally leads to a distribution of T_1 and T_2 signal lifetimes.

$$\frac{1}{T_1} = \rho_1 \frac{S}{V} \tag{1}$$

$$\frac{1}{T_2} = \rho_2 \frac{S}{V} \tag{2}$$

In previous research, we have developed MRI techniques to determine the spatial distribution of water (hydrogen), chlorides, and sodium held within the pore structure of the cement paste matrix in mortars and concretes [5,13]. The short signal lifetimes (short relaxation times) in cement-based materials means imaging is very difficult, if not impossible, with traditional MRI techniques. These difficulties are avoided by the SPRITE class of materials imaging technique [14].

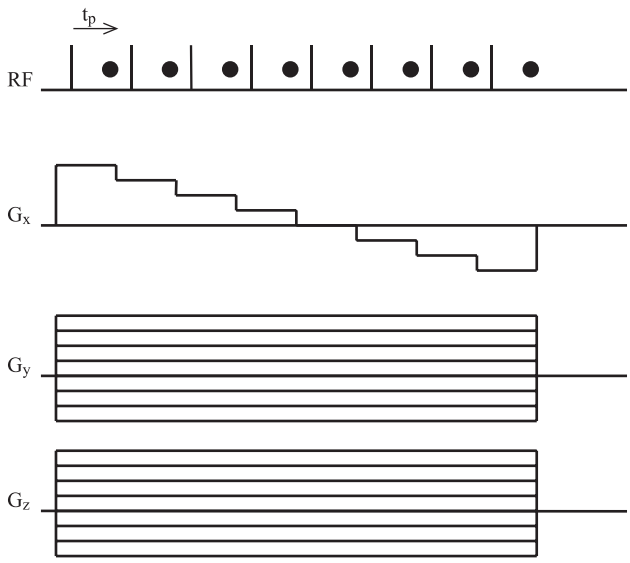

Fig. 1. Three-dimensional SPRITE technique. The magnetic field gradients G_x, G_y, and G_z are cycled through 64, 64, and 32 steps. Data points are acquired at a time t_p after the radio frequency pulse. T_R is the time between RF pulses.

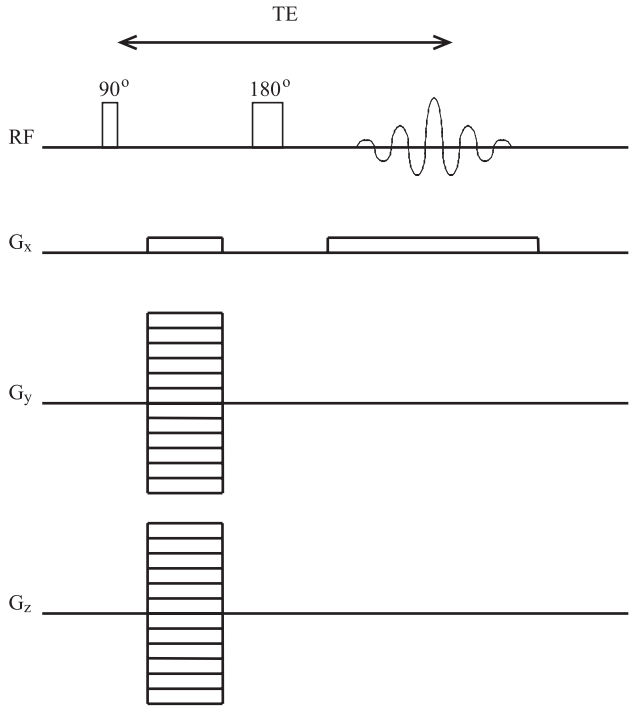

Fig. 2. Three-dimensional spin–echo technique. G_x, G_y, and G_z are frequency and phase encode gradients that acquire 128, 128, and 64 points, respectively. T_E is the time from the 90° pulse to the center of the echo. T_R is the time from one RF 90° pulse to another.

The SPRITE signal intensity [14] at any point within an image is given by Eq. (3); where, ρ_o is the nuclei density, t_p is the phase encoding time, T_R is the repetition time, and α is the rotation angle for sample magnetization excited by a radio frequency (RF) pulse. The variables T_1 and T_2* are the MR relaxation times. Fig. 1 is a schematic diagram of the measurement technique. This technique is ideal for determining the spatial distributions and total water content in cement-based materials; however, it does not permit high-resolution imaging (resolution <1 mm). Because the SPRITE technique does not easily permit high resolution, and signal lifetimes of water in cracks are relatively long, it is not well suited for imaging cracks in cement-based materials.

$$S = \rho_o e^{-\frac{t_p}{T_2^*}} \left(\frac{1 - e^{\frac{-TR}{T_1}}}{1 - \cos\alpha e^{\frac{-TR}{T_1}}} \right) \sin\alpha \tag{3}$$

Cracks in cement paste will have S/V ratios significantly smaller than the water-filled capillary and gel pores translating into longer T_1's and T_2's. The difference in T_1 and T_2 between the water-filled pore structure and water-filled

cracks, can allow for contrast in MR images which in turn will allow for the identification of cracked and uncracked regions. Because the cracking problem manifests itself as T_1 and T_2 contrasts between cracks and the pore structure, the spin–echo imaging technique was selected for investigation. Spin–echo imaging is a standard MRI method described in other literature [4]. In general, spin–echo imaging is not considered an appropriate method for research in cement-based systems because the very short relaxation times of the hydrogen nuclei cannot be detected using this technique. However, the T_2 signal components found in the large pore structure and in cracks will be observed with this technique.

The signal magnitude at any point within a spin–echo image is given by Eq. (4). Where ρ_o is the proton (water) density, T_E is the echo time, and T_R is the repetition time. As before, T_2 is the spin–spin relaxation time, and T_1 is the spin–lattice relaxation time. The proton density and the relaxation times T_1 and T_2 are measurable properties of the sample. The T_E and T_R are measurement parameters, which can be manipulated to emphasize the structure of interest in an image. Fig. 2 is a schematic of the spin–echo technique.

$$S = \rho_o e^{\frac{-TE}{T_2}}\left(1 - e^{\frac{-TR}{T_1}}\right) \quad (4)$$

In addition to the spin–echo technique, a modification was investigated, known as inversion recovery, which allows for the further suppression of signal from water held in the pore structure. Ordinary spin–echo imaging suppresses signal based on T_2. However, given that pore size, S/V ratio, and scales with both T_1 and T_2, it is possible to exploit the T_1 time constant for additional suppression of the background paste signal. The magnitude of the signal at any pointin the object, with the modified spin–echo sequence, is given by Eq. (5). All parameters with the exception of T_{ir}, which is the time delay between 180° and 90° RF pulses, are the same as Eq. (4). Fig. 3 depicts the inversion recovery spin–echo measurement.

$$S = \rho_o e^{\frac{-TE}{T_2}}\left(1 - 2e^{\frac{-T_{ir}}{T_1}}\right) \quad (5)$$

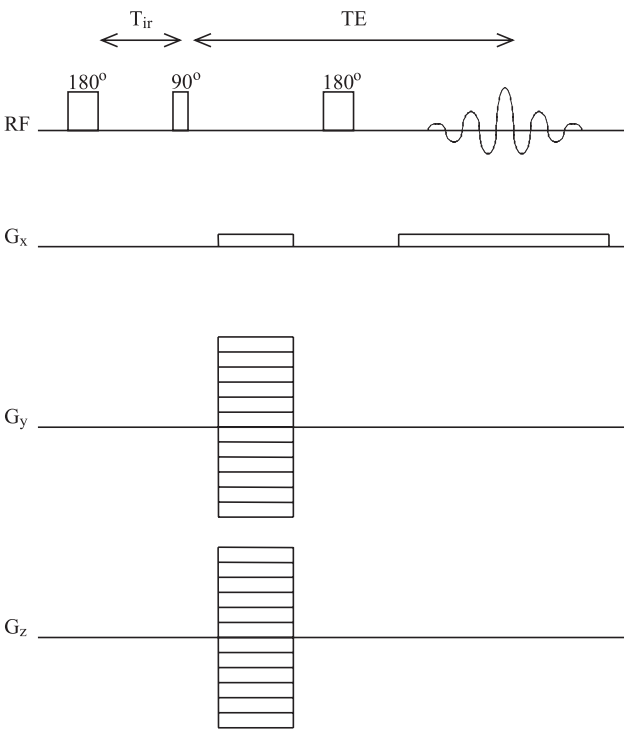

Fig. 3. Inversion recovery spin–echo technique. The measurement is similar to that of Fig. 2, but with the addition of a 180° inversion pulse and delay period T_{ir}. Signal from regions of space with $T_{ir} = \ln 2\ T_1$ are suppressed in the image.

3. Experimental

Two cement paste samples (A and B) were prepared. White portland cement (Federal, Woodstock, ON) was used to prepare cement paste samples with a w/c of 0.6. Specimens were cast into a plastic rectangular mold of dimensions 10 × 10 × 40 mm. The mold was placed on its 10 × 10 mm base and the cement paste was then placed in the mold. The mold was gently tapped to consolidate the paste. While the paste was still plastic, thin sheets of copper, 8 mm wide and 150 μm thick, were inserted 3–4 mm into the top of the two specimens to form synthetic cracks. After 1 day of moist curing, the copper sheets were removed, and the specimens were cut using a diamond saw. Specimen A was cut 10 mm from the cast surface so as to produce a 10 × 10 × 10 mm cube with a synthetic crack on the diagonal of the top surface. Specimen B was cut 5 mm from the cast surface, producing a 10 × 10 × 5 mm cube, also with a synthetic crack on the diagonal of the top surface.

At the time of cutting and subsequent removal of the mold, specimen A was slightly damaged and additional cracks developed. Fig. 4 is a photograph of specimen A. Figs. 5, 6, and 7 are orthogonal views of the top, right front, and left rear respectively. The surface crack widths were measured using a microscope with a scale overlaid on the cracks. The top synthetic crack, depicted in Fig. 5, was estimated to be 300 μm wide. The crack observed in Fig. 6 was estimated to be 100 μm wide. The crack in Fig. 7 was approximately 60 μm thick. Specimen A was immersed in water for approximately 3 months prior to imaging. This conditioning allows for complete hydration (although this is not necessary) and saturation of all cracks.

No additional damage to specimen B was evident at the time of cutting and subsequent demolding. A photograph of the specimen is shown in Fig. 8. The synthetic crack was estimated to be 300 μm wide using a scale and microscope. The specimen was stored in water for 7 days prior to imaging, to allow for saturation of the synthetic crack and partial hydration.

MRI measurements were conducted on a Nalorac (Martinez, CA) 4.7 T, 76 mm bore, superconducting magnet with a 48-mm micrograd ient insert (Doty Scientific, Columbia,

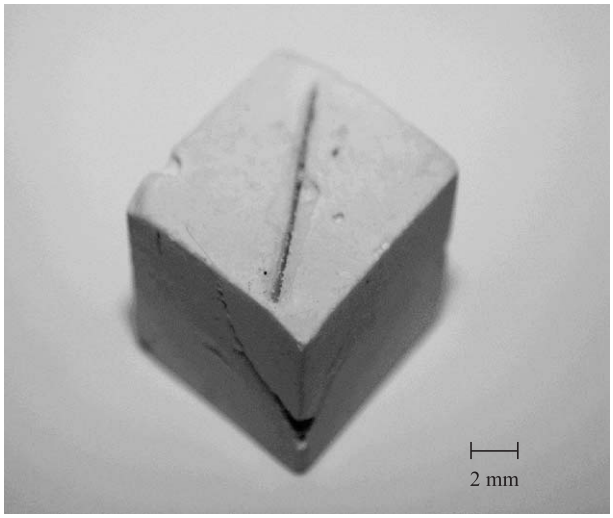

Fig. 4. Photograph of specimen A. The large slot on the top of the photo is the synthetic crack. The crack on the left front and right front of the specimen resulted from damage during demolding.

SC). A Litz type RF probe (Doty Scientific) was used for imaging. The spectrometer console was a Tecmag Apollo (Houston, TX). The probe was driven by a 300-W AMT M3205A RF amplifier (American Microwave Technology, Berea, CA). All MRI measurements were performed at ambient temperature. Image reconstruction and analysis were undertaken in IDL 5.4 (Research Systems, Boulder, CO) with custom software routines.

A 3D SPRITE measurement was performed on specimen A. The total measurement time was 70 min. The field of view was set at $20 \times 20 \times 20$ mm and collected in a $64 \times 64 \times 32$ matrix, resulting in a nominal resolution of $312 \times 312 \times 625$ μm. Four signal averages were collected, with $t_p = 250$ μs, $T_R = 2$ ms, and $\alpha = 9.7°$. Measurements were performed while the specimen was water-saturated.

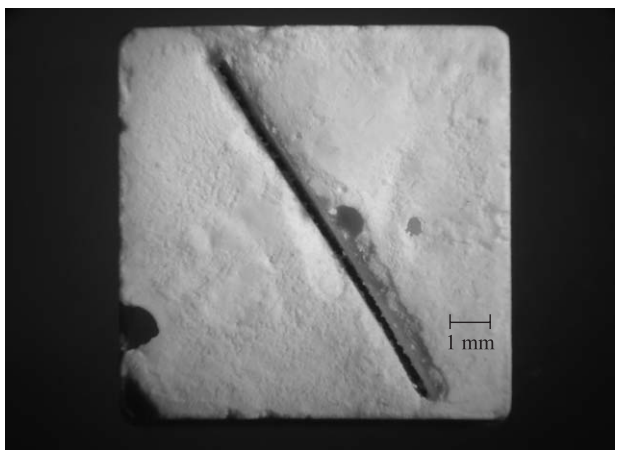

Fig. 5. Photograph of specimen A. Top view showing the synthetic crack. The crack was estimated to be 300 μm wide using a scale and microscope.

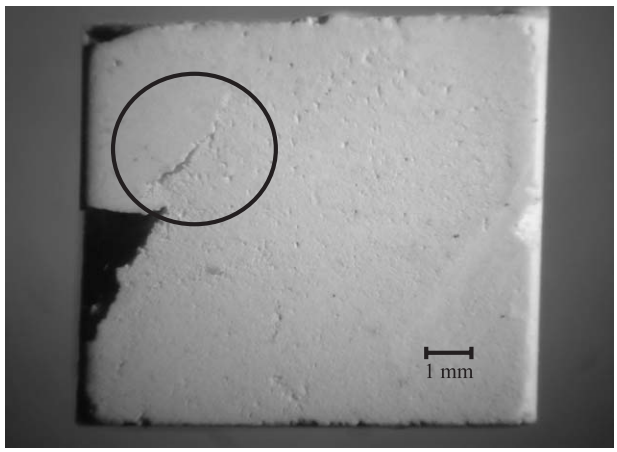

Fig. 6. Photograph of specimen A. A view of the right front, referenced to Fig. 4, showing the crack (inside circle) that formed during demolding. The crack was estimated to be 100 μm wide using a scale and microscope.

Three-dimensional spin–echo and inversion recovery measurements were performed on specimen A. The spin–echo measurement time was 270 min, the field of view was set at $20 \times 20 \times 20$ mm with a $128 \times 128 \times 64$ matrix, resulting in a nominal resolution of $156 \times 156 \times 312$ μm. Four signal averages were collected with a T_E of 2.7 ms and a T_R of 500 ms. A spin–echo measurement with the specimen saturated was followed by an additional measurement after 1 day of drying at ambient laboratory conditions. The inversion recovery spin–echo measurement was performed when the specimen was saturated. The inversion recovery measurement used a T_{ir} of 17.5 ms with all other parameters equivalent to the spin–echo measurement. The measurement time was 280 min.

Specimen B was used for 2D spin–echo and inversion recovery spin–echo measurements. The spin–echo measurement time was 4.5 min. The field of view was set at

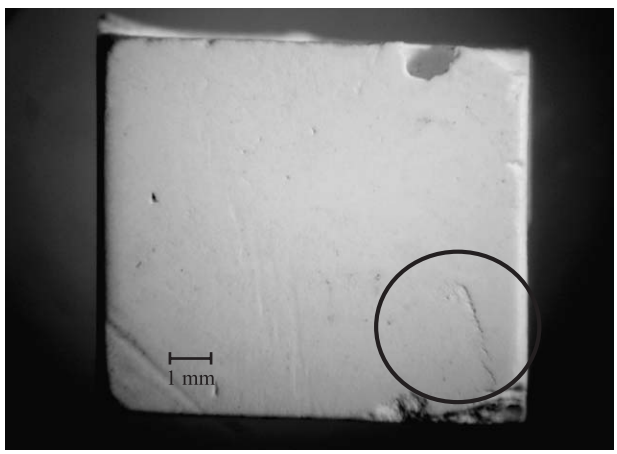

Fig. 7. Photograph of specimen A. A view of the left rear, referenced to Fig. 4, showing an additional crack (inside circle) that formed during demolding. The crack was estimated to be 60 μm wide using a scale and microscope.

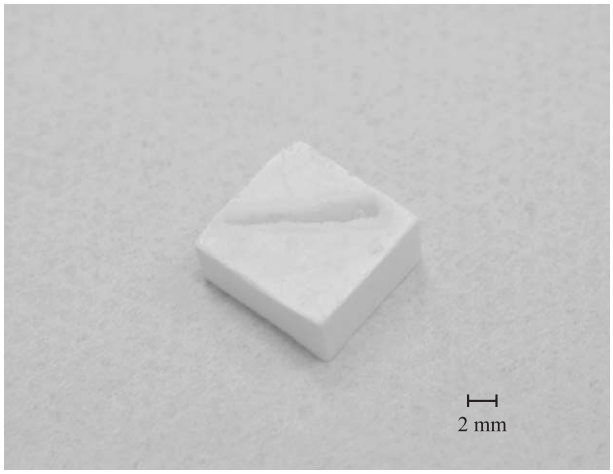

Fig. 8. Photograph of specimen B. The large slot on the top of the photo is the synthetic crack. This crack was estimated to be 300 μm wide using a scale and microscope.

20×20 mm with data collected in a 128×128 matrix, resulting in a nominal resolution of 156×156 μm. The number of signal averages was four, T_E was 2.7 ms, and T_R was 500 ms. The inversion recovery spin–echo measurement had a T_{ir} of 17.5 ms with all other parameters equivalent to the standard technique. Total measurement time was only slightly longer than 4.5 min.

Signal to noise ratios (SNRs) were calculated from 2D images. The calculation is the average signal from one region, such as paste or a crack, divided by the average signal from the background signal region (noise). SNRs were calculated for paste and crack regions for SPRITE, spin–echo, and inversion recovery spin–echo measurements.

4. Results and discussion

The SPRITE MRI technique is well suited for studying materials with short signal lifetimes. Fig. 9 is a 2D slice extracted from a 3D image of specimen A. Three observations can be drawn from this image: there is a strong signal from the paste, the synthetic crack is seen as a void, and the small natural cracks are not visible.

There is a strong signal from the paste and this is readily understood by considering the SPRITE imaging parameters. The encoding time was set at 250 μs with a T_R of 2 ms for these measurements. The T_2* of cement pastes varies; however, from previous work, it is typically on the order of 200 μs for cement paste. The signal from the paste is quite strong even after selecting a longer than normal t_p; this was due to the significant amount of water in the paste (ρ_o). In addition, α is small enough to ensure that the signal contribution associated with the T_1 term in Eq. (3) was approximately 1.

The large synthetic crack was observed to be a signal void, although at the time of measurement, the crack was water-saturated. The signal from water in the crack is suppressed due to the long T_1 of bulk water and the short T_R of the measurement. The relatively long T_1 of bulk water in the crack, through Eq. (3), yields low signal intensity compared to the cement paste with a short T_1. In Fig. 9, the signal ratio from the surrounding paste to the synthetic crack was approximately 3. The features of Fig. 9 may be understood by applying Eq. (3) and coupling the known measurement parameters with the following assumptions: T_1 of the paste, 5 ms; T_1 of the crack, 2000 ms; T_2* of the paste, 200 μs; T_2* of the crack, 2000 μs; ρ_o of the paste, 0.3; and ρ_o of the crack, 1. Eq. (3) suggests water in a crack would produce only 70% of the signal anticipated from paste per unit volume. One must consider this calculation merely as an estimate. The calculation assumes a unique T_1, yet, there is known to be a distribution of T_1's in the specimen.

The geometrical requirements for crack detection in this specimen, using the SPRITE technique, can be estimated. Eq. (6) [4] is the contrast to noise ratio (CNR), where SNR_A and SNR_B are the SNRs of the structures of interest. A CNR of $2\sqrt{2}$ provides a 95% confidence level, that two neighboring voxels (volume element) contain different structures [4]. Assuming that a crack is a sheetlike structure that extends through the depth and length of a voxel and that a CNR of $2\sqrt{2}$ from neighboring voxels is needed to detect a crack, the minimum crack width can be estimated. The SNR for the synthetic crack that is assumed to fill a voxel was 3.4 (Fig. 9). The SNR for a voxel of paste was 9 (Fig. 9). A weighted average of SNR of the crack and paste, coupled with the CNR, can be used to estimate the minimum crack width detectable for this specimen with these measurement parameters. For specimen A and for the SPRITE technique,

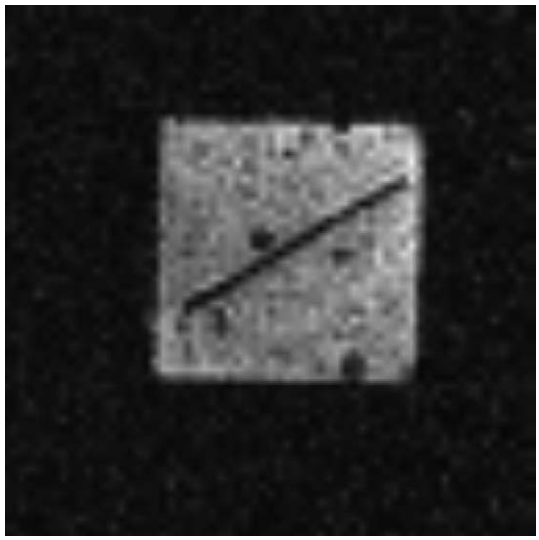

Fig. 9. Two-dimensional slice from a 3D SPRITE image of specimen A. The image-displayed plane is from near the top surface of the sample. Notice that the synthetic crack appears as a rectangular void area. No other cracks are visible in the slice.

the minimum detectable crack width was estimated to be 160 μm.

$$CNR_{AB} = SNR_A - SNR_B \quad (6)$$

Only the large synthetic crack was visible in Fig. 9. The crack shown in Fig. 6 should appear in Fig. 9 as a line crossing the synthetic crack. It is not visible due to the resolution restrictions of the SPRITE method and suppression of the signal from longer components of T_1. The crack in Fig. 6 was only 100 μm wide. When using SPRITE to image cracks, the nominal resolution should be several times finer than the smallest crack. Because water in the crack produces low signal, any overlap of the voxel into paste with short relaxation times will produce a large signal that will obscure any cracks smaller than the nominal resolution.

Figs. 10 and 11 are rendered 3D spin–echo images of the cracks in specimen A. Fig. 10 shows a view similar to that of Fig. 4, with the large slot-like crack on the top of the specimen, and a triangular crack on the foremost corner of the specimen. Also present in this image is the structure of the base and water-filled depressions on the surface of the specimen resulting from condensation in the specimen holder. Fig. 11 is a rotated version of Fig. 10 showing the crack presented in Fig. 7.

Spin–echo imaging produces images with T_1 and T_2 contrasts according to Eq. (4). Spin–echo imaging will suppress signal from short T_2's in paste due to the parameter T_E through the second term of Eq. (4). It is for this very reason that spin–echo imaging is not appropriate for general water-content measurements in cement-based systems. The T_2's are too short to be observed because hardware restrictions do not allow for short enough echo times. In Fig. 10, the signal ratio of water in the synthetic crack to paste was

Fig. 10. Three-dimensional rendered spin–echo image of specimen A. The image orientation is similar to that of Fig. 4. The large synthetic crack is visible as well as the triangular crack of Fig. 6. The bottom of the image shows the rectangular structure of the specimen as a result of water condensing on the specimen surface. Droplet structures in the image are water condensed in the surface defects of the specimen.

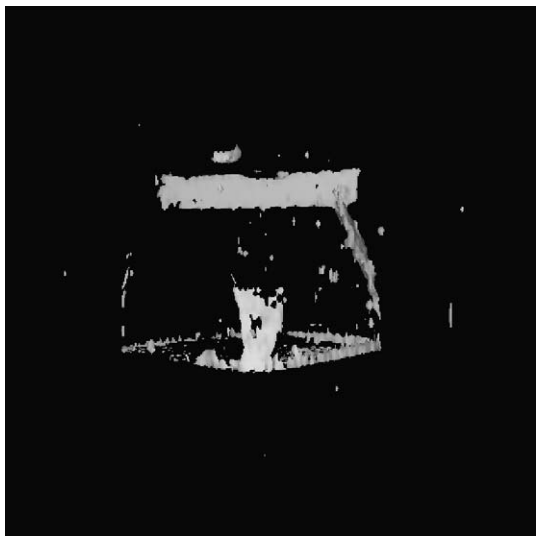

Fig. 11. Three-dimensional rendered spin–echo image of specimen A. This view of the image shows the crack of Fig. 7. Also present are the synthetic crack on the top of the specimen, the triangular crack, and water filling the surface defects of the specimen.

9, the signal ratio for the 100-μm crack to paste was 9, and the signal ratio for the 60-μm crack to paste was 3. To better understand the spin–echo image, Eq. (4) was applied with the following assumptions: T_1 of the paste, 5 ms; T_1 of the crack, 2000 ms; T_2 of the paste, 2 ms; T_2 of the crack, 200 ms; ρ_o of the paste, 0.3; and ρ_o of the crack, 1. These values predict that paste yields only 35% of the signal that was predicted for water in a crack. Once more, this calculation is an estimate as there are distributions of both T_1 and T_2.

The CNR criteria that was used to predict the minimum detectable crack width for the SPRITE technique can be used to predict the minimum crack width in the 3D spin–echo measurement of specimen A. The SNR for the synthetic crack that is assumed to fill a voxel was 10.7 (Fig. 10). The SNR for a voxel of paste was 1.2 (Fig. 10). Based on the weighted average of the SNR coupled with the CNR, we estimate that a crack width of 50 μm could be detected in specimen A using the 3D spin–echo measurement.

To test the sensitivity of the 3D spin–echo measurement to sample saturation, specimen A was dried at ambient laboratory conditions overnight on the bench top. The specimen was imaged the next day using the same spin–echo measurement parameters. No structure was observed in the image due to the removal of water held in the cracks by drying.

Specimen B was moist-cured for only 7 days and has a high w/c. Therefore, it has a large pore size distribution when compared with a fully hydrated sample and lower w/c [12]. This large pore size distribution will translate into longer T_1's and T_2's. Fig. 12 is the 2D spin–echo image of specimen B. The image shows a bright line in the image center that corresponds to the synthetic crack shown in Fig. 8. Also present in the image is a bright signal from the surrounding paste. The ratio of signal from the crack to signal from the paste is approximately 3 with an SNR of 40

for the crack. While it is possible to distinguish a large crack, a crack that is smaller than the nominal pixel resolution would likely be obscured by the strong background paste signal (i.e., low-intensity signal on top of high-intensity signal).

Application of inversion recovery coupled with the spin–echo technique can be used to suppress selected T_1 components of the paste, therefore reducing the signal from paste still further compared to spin–echo imaging alone. Fig. 13 is a 2D image of specimen B acquired using the inversion recovery spin–echo technique. Examination of the image shows that most of the signal from the paste is suppressed, while the crack remains an intense image feature. The ratio of signal from the crack to signal from the paste is 12 with an SNR of 42 for the crack. When compared to the 2D spin–echo image, this is an improvement of paste signal suppression by a factor of 4 without adversely changing the overall signal to noise.

The inversion recovery feature will zero portions of the signal with $T_1 = T_{ir}/\ln 2$. In our case, T_1's around 25 ms are therefore set to zero in the image. A multiexponental analysis was carried out to determine the T_1 and T_2 of specimen B. The results indicated a bimodal distribution of relaxation times with two principal T_1 components, 10 and 2000 ms. T_2 was also bimodal with two principal components, 1 and 200 ms. Using these values with Eq. (5), a crack would be expected to yield a signal 100 times greater than the paste. This calculation is once more an estimate due to the distribution of T_1's and T_2's which are known to be present.

The 3D inversion recovery measurement of specimen A can be used to estimate the minimum crack width that can be detected in specimen A. Using the previous CNR

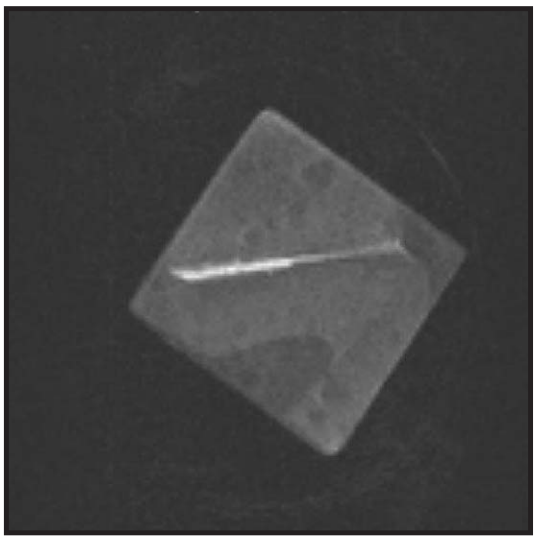

Fig. 12. Two-dimensional spin–echo image of specimen B. This is a similar view to Fig. 8. This image shows the water-filled synthetic crack as well as a significant signal from the cement paste structure. The ratio of signal from the crack to signal from the paste is 3. The ratio of signal from the crack to background signal is 40. The signal in a 2D image is an average over the in-plane depth of the specimen.

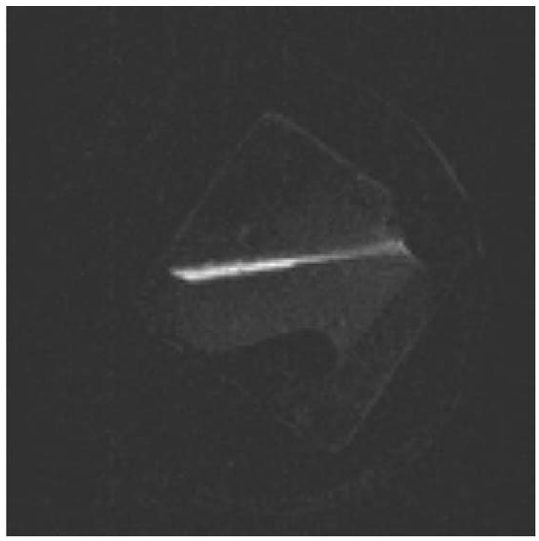

Fig. 13. Two-dimensional inversion recovery spin–echo image of specimen B. The view is similar to Fig. 8. This image shows the very strong signal from the synthetic crack and suppression of signal from the paste. The ratio of signal from the crack to signal from the paste is 12. The ratio of signal from the crack to signal from the background is 42.

methodology, with the measured SNR of 1.3 for paste and the SNR of 35.9 for the synthetic crack, a 15-μm minimum crack thickness should be observable for specimen A using inversion recovery methods. This is more than a threefold improvement in resolution over the simple spin–echo measurement.

The nominal resolution of these images naively appears to be too coarse for application to concrete material research. While this is true from a pure geometry point of view, the spin–echo and inversion recovery techniques are only sensitive to long T_1's and T_2's and therefore, the signal will only be observed from water-filled cracks or other water-filled structures in the sample. Because cracks have lengths that typically extend at least over several voxel lengths, this connectivity may be exploited for visual identification of crack structures, even if their widths are less than the nominal resolution.

Returning to the definition of Hornain et al. [2] of an ideal crack detection methodology, MRI meets most of the characteristics of a good technique to study cracking in concrete samples. It is nondestructive, it is relatively simple and economic (if one has access to MRI instruments), the initial state of the material can be characterized, and it is coupled with an image analysis system.

5. Conclusions

The spin–echo technique successfully imaged water held in the cracks of a hydrated cement paste sample. In addition to the standard spin–echo technique, inversion recovery was applied to further suppress signal obtained from the large water-filled structures in cement paste. While spin–echo

imaging works very well to localize water-filled cracks, it is very dependent on the degree of saturation of these cracks and it is not suitable for spatially resolving water in capillary and gel pores. These techniques can be used to resolve cracks much smaller than the nominal resolution of the measurement by relying on the connectivity of the crack structure, and on the fact that it is relatively easy to detect a high-intensity structure on a low-intensity background.

The SPRITE imaging technique is able to spatially resolve the distribution of water in cement paste; however, due to resolution and signal suppression issues, it is not well suited to the study of small water-filled cracks in cement-based systems.

The obvious extension of this work is to apply this methodology to study the formation of cracks in cement paste subjected to cycles of freezing and thawing. These studies are in progress.

Acknowledgements

This work was supported by equipment and operating grants awarded to BJB by NSERC of Canada. BJB thanks NSERC for a Steacie Memorial fellowship (2000–2002) and the Canada Chairs program for a Tier 1 Research Chair. JJY thanks NSERC for a postgraduate scholarship.

References

[1] S. Jacobsen, J. Marchand, L. Boisvert, Effect of cracking and healing on chloride transport in opc concrete, Cem. Concr. Res. 26 (4) (1996) 869–881.

[2] H. Hornain, J. Marchand, A. Ammouche, J.P. Commene, M. Moranville, Microscopic observation of cracks in concrete—a new sample preparation technique using dye impregnation, Cem. Concr. Res. 26 (4) (1996) 573–583.

[3] E. Ringot, J.P. Ollivier, J.C. Maso, Characterisation of initial state of concrete with regard to micro cracking, Cem. Concr. Res. 17 (3) (1987) 411–419.

[4] E.M. Haacke, R.W. Brown, M.R. Thompson, R. Venkatesan, Magnetic Resonance Imaging Physical Principles and Sequence Design, Wiley, New York, 1999.

[5] S.D. Beyea, B.J. Balcom, T.W. Bremner, P.J. Prado, D.P. Green, R.L. Armstrong, P.E. Grattan-Bellow, Magnetic resonance imaging and content profiles of drying concrete, Cem. Concr. Res. 28 (3) (1998) 453–463.

[6] S.D. Beyea, B.J. Balcom, T.W. Bremner, P.J. Prado, A.R. Cross, R.L. Armstrong, P.E. Grattan-Bellow, The influence of shrinkage-cracking on the drying behaviour of white portland cement using Single-Point Imaging (SPI), Solid State Nucl. Magn. Reson. 13 (1998) 93–100.

[7] R.L. Kleinberg, W.E. Kenyon, P.P. Mitra, Mechanism of nmr relaxation of fluids in rock, J. Magn. Reson., Ser. A 108 (1994) 206–214.

[8] A. Plassais, M.P. Pomies, N. Lequeux, P. Boch, J.P. Korb, Micropore size analysis in hydrated cement paste by NMR, Magn. Reson. Imaging 19 (2001) 493–495.

[9] J.Y. Jehng, D.T. Sprague, W.P. Halperin, Pore structure of hydrating cement paste by magnetic resonance relaxation analysis and freezing, Magn. Reson. Imaging 14 (7/8) (1996) 785–791.

[10] W.P. Halperin, J.Y. Jehng, Y.Q. Song, Application of spin–spin relaxation to measurement of surface area and pore size distributions in hydrating cement paste, Magn. Reson. Imaging 12 (2) (1994) 169–173.

[11] S.D. Beyea, B.J. Balcom, T.W. Bremner, R.L. Armstrong, P.E. Grattan-Bellow, Detection of drying induced microcracking in cementitious materials with spatially resolved 1H nuclear magnetic resonance relaxometry, J. Am. Ceram. Soc. 86 (2003) 800–805.

[12] D. Winslow, D. Liu, The pore structure of paste in concrete, Cem. Concr. Res. 20 (2) (1990) 227–235.

[13] F. de J. Cano, T.W. Bremner, R.P. McGregor, B.J. Balcom, Magnetic resonance imaging of ^{1}H, ^{23}Na, and ^{35}Cl penetration in Portland cement mortar, Cem. Concr. Res. 32 (2002) 1067–1070.

[14] B.J. Balcom, R.P. MacGregor, S.D. Beyea, D.P. Green, R.L. Armstrong, T.W. Bremner, Single-point ramped imaging with T_1 enhancement (SPRITE), J. Magn. Reson., Ser. A 123 (1996) 131–134.